







RESEARCH ARTICLE | JUNE 27 2024

Simple model of multi-scale and multi-site emissions for porous ionic liquid electro spray thrusters

Koki Takagi   ; Yusuke Yamashita  ; Ryudo Tsukizaki  ; Kazutaka Nishiyama  ; Yoshinori Takao 



J. Appl. Phys. 135, 244502 (2024)

<https://doi.org/10.1063/5.0195699>



Journal of Applied Physics
Special Topic:
**Phonon-Magnon Interactions:
From Fundamentals to Device Physics**
Guest Editors: Vasily V. Temnov, Alexey V. Scherbakov, Yoshi Chika Otani, Paolo Vavassori
[Submit Today!](#)



Simple model of multi-scale and multi-site emissions for porous ionic liquid electro spray thrusters

Cite as: J. Appl. Phys. **135**, 244502 (2024); doi: [10.1063/5.0195699](https://doi.org/10.1063/5.0195699)

Submitted: 3 January 2024 · Accepted: 31 May 2024 ·

Published Online: 27 June 2024



Koki Takagi,^{1,2,a)}  Yusuke Yamashita,²  Ryudo Tsukizaki,³  Kazutaka Nishiyama,³  and Yoshinori Takao^{4,b)} 

AFFILIATIONS

¹Department of Mechanical Engineering, Materials Science, and Ocean Engineering, Yokohama National University, Yokohama 240-8501, Japan

²Department of Aeronautics and Astronautics, The University of Tokyo, Bunkyo-ku, Tokyo 113-8656, Japan

³Institute of Space and Astronautical Science, Japan Aerospace Exploration Agency, Sagami-hara 252-5210, Japan

⁴Division of Systems Research, Yokohama National University, Yokohama 240-8501, Japan

^{a)}Author to whom correspondence should be addressed: takagi-koki-zn@ynu.jp

^{b)}takao@ynu.ac.jp

ABSTRACT

Ionic liquid electro spray thrusters represent an alternative propulsion method for spacecraft to conventional plasma propulsion because they do not require plasma generation, which significantly increases the thrust efficiency. The porous emitter thruster has the advantages of simple propellant feeding and multi-site emissions, which miniaturize the thruster size and increase thrust. However, the multi-scale nature, that is, nano- to micrometer-sized menisci on the millimeter-size porous needle tip, makes modeling multi-site emissions difficult, and direct observation is also challenging. This paper proposes a simple model for multi-site emissions, which assumes that the ionic conductivity or ion transport in the porous media determines the ion-emission current. The conductivity was evaluated by comparing the experimental and numerical data based on the model. The results suggest that the ionic conductivity of the porous emitter is suppressed by the ion-pore wall friction stress. Additionally, the model indicates that the emission area expansion on the porous emitter creates the unique curve shape of the current vs voltage characteristics for multi-site emissions.

© 2024 Author(s). All article content, except where otherwise noted, is licensed under a Creative Commons Attribution-NonCommercial-NoDerivs 4.0 International (CC BY-NC-ND) license (<https://creativecommons.org/licenses/by-nc-nd/4.0/>). <https://doi.org/10.1063/5.0195699>

I. INTRODUCTION

Electro spray thrusters, which extract ions directly from a liquid propellant without generating plasma, have attracted considerable attention for small spacecraft systems because of their high propulsion efficiency, even in low-power operations (e.g., a few watts). Electro spray thrusters were first developed as colloid thrusters,¹ which achieve large thrust but low specific impulses. Recently, ionic liquids (ILs), which are molten salt at room temperature, have been developed.² If thrusters emit ions from the IL of the propellant at higher speeds, they achieve higher specific impulses with smaller thrusts.³ This operation mode, which is called “purely ionic regime,” is useful for long-term operation.^{4–6} These IL electro spray thruster technologies have introduced the possibility of large

increments of spacecraft velocity for maneuver ΔV even for small and low-power spacecraft.⁷

Three basic types of IL electro spray thrusters with different emitter structures have been proposed: capillary,^{8–10} externally wetted,^{3,11,12} and porous.^{13,14} The porous type can be easily manufactured via mechanical machining^{15–18} and allows the propellant feeding system to be simple and small. It can also easily achieve a purely ionic regime.^{19,20} In addition, it can utilize multi-site emission, which enhances the thrust. The emission region is large on the needle tip, with many emission sites. The multiple menisci may be generated by periodic internal pressure owing to various pores or instability of ILs on the porous surface.^{21–23} Thus, the relatively large tip curvature of the emitter needle tip potentially induces

28 June 2024, 00:02:15

multi-site emission and increases the thrust, rather than a completely sharp emitter geometry.^{18,21}

There are large differences in the physics scale in porous IL emission. Figure 1 shows the multi-scale of porous IL electro spray thrusters: (a) an entire thruster head (≈ 1 cm) has many porous emitters, (b) one porous needle typically has a size less than 1 mm, and (c) IL menisci with sizes of 1 nm–1 μ m appear on the porous needle tip, leading to the multi-site emissions. There are 10^3 - to 10^6 -order size differences between the emitter needle and menisci.

An empirical model,²⁴ a statistical prediction model,²⁵ and a combination of numerical simulations^{26,27} have been used to describe the emissions. However, the physical modeling of multi-site emission is unclear. Accurately predicting the current emitted from porous emitters and reproducing the current vs voltage (I - V) characteristics have been challenging owing to the complex geometry of IL menisci on the porous emitter needle. Optical observation of the menisci is close to or below the diffraction limit, and electron microscopy also resulted in limited success because high-energy electrons caused the solidification of the IL.²⁸

In this study, the proposed model predicted the current emitted from the porous emitter using the surface electric field on the needle, which can be calculated as the solution of Laplace's equation. The current-voltage (I - V) characteristics are reproduced using the model, avoiding multi-scale complexity. For the modeling, we focus on the assumption that ionic conductivity determines ion emission rather than ion evaporation. References 29 and 30 have reported that conductivity significantly affects ion emissions.

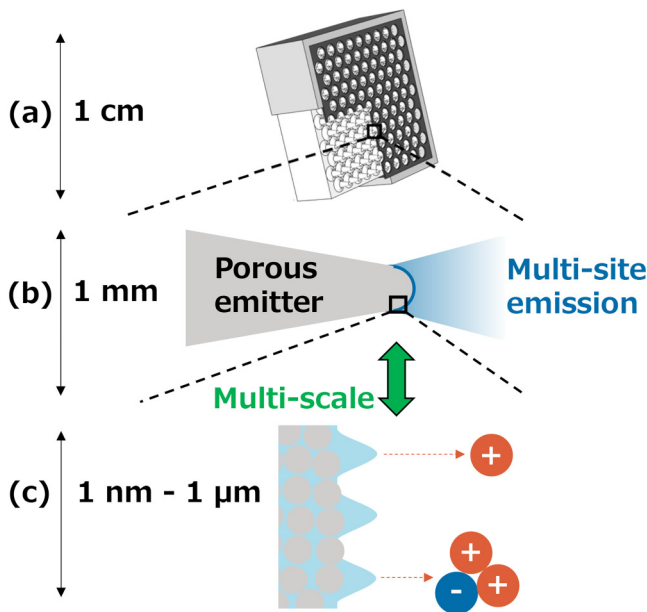


FIG. 1. The multi-scale property of a porous IL electro spray thruster is described as follows: (a) An entire thruster head (≈ 1 cm), (b) one porous emitter in the thruster (≈ 1 mm), and (c) IL menisci on the porous needle tip (≈ 1 nm–1 μ m).

The proposed model for describing emitted current density j_{em} incorporates ionic conductivity κ suppressed by porous media (model parameter) with the surface electric field E_{surf} on the porous needle and the threshold surface electric field $E_{surf,th}$ for emission. The total emitted current I_{em} can be calculated via the area integration of the emitted current density j_{em} . The conductivity κ was evaluated using the calculated surface electric field E_{surf} and the measured total emitted current I_{em} . The threshold electric field $E_{surf,th}$ was also obtained via experiments. The detailed electric equations are described in Sec. II.

The model successfully simulated the I - V characteristics using a constant ionic conductivity for 7 μ m class porous emitters, where the expansion of the emission area resulted in the curve shape corresponding to the multi-site emission. The proposed physical model also explains the role of porous media in emission. The ion-pore wall friction stress restricts the ionic conductivity in the porous media, and the conductivity determines the emitted current.

II. MODELING

A. Ion evaporation

Ions of the IL in the porous needle emitter are transported to the needle tip. Multiple IL menisci are generated on the surface of the needle tip. Ions are evaporated on the menisci tips as shown in Fig. 2(a). The evaporation from the IL surface is described by the kinetic process,^{31,32} as shown in Fig. 2(b),

$$j = \sigma \frac{k_B T}{h} \exp \left[-\frac{\Delta G - G(E_v)}{k_B T} \right], \quad (1)$$

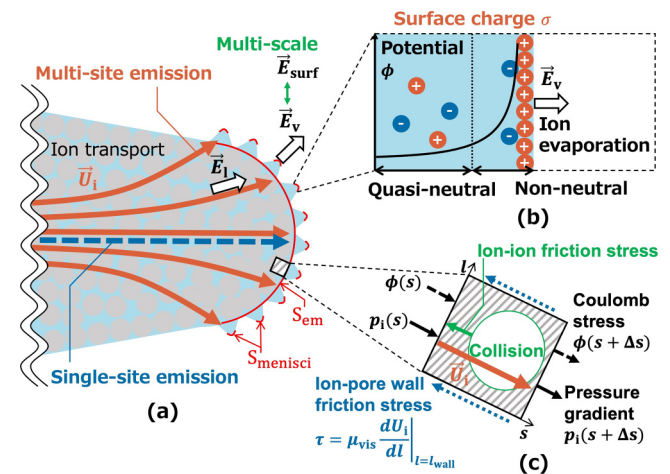


FIG. 2. (a) The global ion transport of the IL in the porous emitter needle and menisci on the needle. The spread and non-spread streamlines of ions indicate multi-site and single-site emissions, respectively. Ions are not supplied to surfaces far from the tip when ions are not easily transported. (b) Structure of the surface charge of the IL. A non-neutral region and a quasi-neutral region are formed. (c) Stresses applied to ions in the porous emitter for momentum conservation as a continuum model.

28 June 2024 00:02:15

where σ represents the surface charge density; k_B represents the Boltzmann constant; T represents the temperature of the IL; h is Planck's constant; E_v represents the electric field on the IL surface; $G(E_v)$ represents the reduction of the energy barrier due to E_v , which is described as $G(E_v) = (e^3 E_v / 4\pi\epsilon_0)^{1/2}$ for polar media based on the Schottky hump; ΔG represents the evaporation energy barrier for solvation;³¹ and ϵ_0 is the electric constant. There are almost no emissions without an electric field because $\Delta G/k_B T \ll 1$, and emission is observed when $\Delta G - G(E_v) = O(k_B T) \ll \Delta G$, e.g., when

$$E_v = \frac{4\pi\epsilon_0(\Delta G)^2}{e^3} \equiv E_v^*, \quad (2)$$

where E_v^* is defined as the threshold electric field for ion evaporation.³⁰ This indicates that a strong electric field $E_v^* \approx 2 \times 10^9$ V/m is needed for emission, which is calculated with $\Delta G \approx 2$ eV.^{4,32} Equation (1) is valid when $\Delta G > G(E_v)$, i.e., $E_v < E_v^*$. When $E_v > E_v^*$, all ions arriving at the meniscus tip are evaporated. Thus, the current is limited by the current density in the porous media upstream from the meniscus.

B. Ion transport in porous media

The ion transport is described with momentum conservation as a continuum model with porous media.^{33,34} The momentum conservation consists of inertial stress, Coulomb stress, ion-ion friction stress, ion-pore wall friction stress, and pressure gradient as shown in Fig. 2(c),

$$m_i n_i \frac{D\vec{U}_i}{Dt} = q_i n_i \vec{E}_i - m_i n_i R_l (\vec{U}_i - \vec{U}_n) - \tau - \vec{\nabla} p_i, \quad (3)$$

where m_i represents the mass of the ions, \vec{U}_i represents the fluid velocity of the ions, \vec{U}_n represents the velocity of opposite polarity ions not used for evaporation, q_i represents the charge of the ions, \vec{E}_i represents the electric field in the IL, R_l represents the coefficient of ion-ion friction stress, τ represents the ion-pore wall friction stress due to the porous internal wall, p_i represents the isotropic ion pressure, and n_i is the concentration (i.e., the number density of ions). Assuming a Newtonian fluid, the shear stress is proportional to the velocity gradient.³⁵ If the velocity on the wall U_{wall} is also assumed to be zero (no-slip condition),³⁶ the ion-pore wall friction stress is proportional to U_i ,

$$\tau = \mu_{\text{vis}} \left. \frac{dU_i}{dl} \right|_{l=l_{\text{wall}}} \approx \mu_{\text{vis}} \frac{U_i - U_{\text{wall}}}{\Delta l} \equiv m_i n_i R_p U_i, \quad (4)$$

where l denotes the axis perpendicular to the ion flow; μ_{vis} represents the viscosity; U_{wall} represents the fluid velocity on the porous wall; and Δl represents the boundary-layer thickness for the wall friction, which is assumed to be constant and thin; and R_p is the ion-pore wall friction stress coefficient.

The number density n_i of both the anions and cations are estimated as $n_i \equiv n_0 \approx \rho/m_{\text{ave}} = 3.7 \times 10^{27} \text{ m}^{-3}$ in the IL, where $\rho = 1.1 \text{ g/cm}^3$ is the density and $m_{\text{ave}} = 88.6 \text{ g/mol}$ is the averaged

mass of ions. In a steady state, \vec{U}_n is negligible, and the inertial term is assumed to be negligible compared with the ion-ion friction stress and ion-pore wall friction stress. The current density in the IL can be expressed using a drift-diffusion model as follows:

$$\vec{j}_i = n_i q_i \vec{U}_i = \mu_i n_i q_i \vec{E}_i - \frac{\mu_i}{q_i} \vec{\nabla} p_i, \quad (5)$$

where μ_i represents the mobility,

$$\mu_i = \frac{q_i}{m_i(R_l + R_p)}. \quad (6)$$

If we ignore the ion pressure gradient, Ohm's law is valid because the ions are the current carriers in the ILs,^{37,38}

$$\vec{j}_i = \kappa \vec{E}_i, \quad (7)$$

where κ represents the ionic conductivity in porous media,

$$\kappa \equiv \mu_i n_i q_i. \quad (8)$$

The above equation indicates that κ decreases with increasing ion-pore wall friction R_p in the porous emitter. When ion-pore wall friction is absent ($R_p = 0$), the conductivity κ corresponds to the intrinsic IL conductivity κ_{IL} . For 1-ethyl-3-methylimidazolium dicyanamide (EMI-DCA), this implies that $\kappa \approx \kappa_{\text{IL}} = 1.8 \text{ S/m}$. Thus, R_l is estimated as $R_l = 3.7 \times 10^{14} \text{ s}^{-1}$ using Eqs. (6) and (8).

C. Connection between ion evaporation and ion transport in porous media

At the bottom of the menisci, the current density of Ohm's law in the IL flowing through porous media [Eq. (7)] and the evaporated current density from the IL surface [Eq. (1)] are related to current conservation and Gauss's law,^{30,39,40}

$$\sigma = \epsilon_0(E_v - \epsilon_r E_l), \quad (9)$$

where ϵ_r is the dielectric constant of the IL, and the surface charge region shown in Fig. 2(b) is assumed to be thin enough, indicating that the surface charge areas of the vacuum side and liquid side are identical.⁴¹ Consider a connection between ion transport and ion evaporation with three electric field ranges: $E_v < E_v^*$, $E_v = E_v^*$, and $E_v > E_v^*$.

When $E_v < E_v^*$, the IL-vacuum boundary condition of j is expressed using Eqs. (1) and (7) as follows:

$$j = \frac{\kappa E_v}{\epsilon_r} \left(1 + \chi \exp \left[\frac{\Delta G - G(E_v)}{k_B T} \right] \right)^{-1}, \quad (10)$$

where χ represents the ratio of the kinetic emission time $h/k_B T$ to the characteristic charge relaxation time $\epsilon\epsilon_0/\kappa$. When $\kappa = 1 \text{ S/m}$, $T = 300 \text{ K}$, and $\Delta G = 2 \text{ eV}$, χ is calculated as $\chi \approx h\kappa/\epsilon_r\epsilon_0 k_B T \approx 2.0 \times 10^{-3} \ll 1$ owing to the lower conductivity of ILs than those of liquid metals.³⁰ Thus, the conductivity

determines the emissions, as assumed by Higuera.²⁹ Ion emissions from a single Taylor cone with changing shapes have been comprehensively investigated in this electric field range ($E_v < E_v^*$).^{42,43}

When $E_v = E_v^*$, the characteristic emitted current density j^* is expressed by Eq. (10) as

$$j^* = \frac{\kappa}{\epsilon_r} \frac{E_v^*}{1 + \chi} \approx \frac{\kappa}{\epsilon_r} \left(E_v^* - \frac{\sigma^*}{\epsilon_0} \right), \quad (11)$$

where $\sigma^* = \epsilon_0 E_v^* \chi \approx 5.0 \times 10^{-5} \text{ C/m}^2$, which indicates that the current density has an offset of σ^*/ϵ_0 .

When $E_v > E_v^*$, the current density is still restricted by Ohm's law, i.e., $j = \kappa E_1$ because of $\chi \ll 1$. In addition, as Gauss's law [Eq. (9)] is also valid, the current density can be expressed by the same formula of Eq. (11),

$$j = \frac{\kappa}{\epsilon_r} \left(E_v - \frac{\sigma}{\epsilon_0} \right). \quad (12)$$

In Eq. (12), the surface charge σ should be self-consistently determined by the balance between the ion transport from the porous media and the evaporation. Figure 2(b) shows the surface charge as the non-neutral region. The non-neutral region (double layer) of ILs may be on the order of nanometers.^{44–47} However, its detailed structure is unclear. The Debye length $\lambda_D = (\epsilon_r \epsilon_0 k_B T / 2q^2 n_0)^{1/2} \approx O(10^{-10}) \text{ m}$ is smaller than the IL ion size. This discrepancy is explained by the electrostatic effect and the steric effect.⁴⁸ The IL has a complex large molecular structure and high binding energies that are comparable to those of covalent bonds.⁴⁹ A non-neutral region is formed near the interface, and the interior becomes quasi-neutral, as shown in Fig. 2(b). The order of the surface charge is $O(\sigma/\epsilon_0) = O(E_v)$ according to Eq. (9) because $E_v \gg \epsilon_r E_1$, as E_1 is small in the quasi-neutral region. In the present work, σ is assumed to be constant for simplicity; i.e., the non-neutral region cannot continue to be expanded with no limit by the increase in the applied electric field, which may differ from the case of $E_v \leq E_v^*$.

D. Multi-scale property between menisci and porous needle

Ion emission starts at approximately $E_v = E^* \approx 2 \times 10^9 \text{ V/m}$. However, the emission begins when the surface electric field on the porous needle (denoted as E_{surf}) reaches approximately $2 \times 10^7 \text{ V/m}$, which is two orders of magnitude smaller than E_v^* . This discrepancy of electric fields is due to the formation of small menisci tips on the porous needles. The electric field at the menisci tips E_v is enhanced up to $E_v = S_{\text{menisci}} E_{\text{surf}} / S_{\text{em}}$ considering Gauss's law under the condition of no space and surface charge, where S_{menisci} is the total area of menisci tips emitting ion, and S_{em} is the emission area of the porous needle surface, as shown in Fig. 2(a). Here, E_{surf} represents the surface electric field on the emitter surface under the condition of no space and surface charge. According to the current conservation, the current density emitted from the porous emitter j_{em} satisfies $j_{\text{em}} S_{\text{em}} = j S_{\text{menisci}}$. When $E_v \leq E_v^*$, the emitted current density j_{em} is expressed by Eq. (10) as

$$j_{\text{em}} = \frac{\kappa E_{\text{surf}}}{\epsilon_r} \left(1 + \chi \exp \left[\frac{\Delta G - G(E_v)}{k_B T} \right] \right)^{-1}. \quad (13)$$

In this study, because we assume $k_B T / \Delta G \ll 1$, the emitted current density j_{em} is negligible; i.e., $j_{\text{em}} \approx 0$ when $E_v \leq E_v^*$. In addition, when $E_v > E_v^*$, the emitted current density j_{em} is expressed by Eq. (12) as

$$j_{\text{em}} = \frac{S_{\text{menisci}}}{S_{\text{em}}} \cdot \frac{\kappa}{\epsilon_r} \left(E_v - \frac{\sigma}{\epsilon_0} \right) = \frac{\kappa}{\epsilon_r} (E_{\text{surf}} - E_{\text{surf,th}}), \quad (14)$$

where $E_{\text{surf,th}}$ represents the offset of E_{surf} interpreted as the threshold of E_{surf} for emission, which is defined as

$$E_{\text{surf,th}} \equiv \frac{\sigma}{\epsilon_0} \cdot \frac{S_{\text{menisci}}}{S_{\text{em}}}. \quad (15)$$

E. Proposed model

On the basis of Eqs. (13) and (14), a model for predicting the current emitted from the porous emitter needle is proposed. Equation (14) is applicable, assuming that sufficient current density exists upstream from the meniscus. Under this assumption, only the local surface electric field E_{surf} determines the emission area S_{em} by $E_{\text{surf}} > E_{\text{surf,th}}$. The current density j_{em} emitted from S_{em} is expressed as

$$j_{\text{em}}(r) = \begin{cases} \frac{\kappa}{\epsilon_r} [E_{\text{surf}}(r) - E_{\text{surf,th}}], & (E_{\text{surf}}(r) > E_{\text{surf,th}}), \\ 0, & (E_{\text{surf}}(r) \leq E_{\text{surf,th}}), \end{cases} \quad (16)$$

where r is the radial coordinate. The proposed model implies that κ is constant and independent of the local electric field. The assumption is valid when the following two conditions are satisfied: (i) the temperature is constant, and (ii) sufficient ions are transported to the porous surface. Regarding (i), κ has been reported to be the function of temperature ($\kappa = \kappa(T)$), and Joule heating increases T .^{39,50,51} However, Joule heating only makes T near the meniscus tip 3%–5% higher than that at the meniscus bottom.³⁹ In this study, the T of the IL in the porous emitter is assumed to be constant, for simplicity. Regarding (ii), when insufficient ions are transported to the porous surface as a global flow in the emitter needle, the emission area on the porous needle may be restricted, and Eq. (16) is invalid. The restricted emission area smaller than S_{em} of the model underestimated κ and induced a non-constant κ (see Sec. IV C).

The total multi-site emission current per needle I_{em} is calculated via area integration of Eq. (16),

$$I_{\text{em}} = \int_{S_{\text{em}}} j_{\text{em}}(r) dS. \quad (17)$$

The needle surface geometry is expressed in terms of the surface position z_{em} as

$$z_{\text{em}} = \begin{cases} \sqrt{R_{\text{tip}}^2 - r^2} + h_{\text{em}} - R_{\text{tip}}, & (0 < r < R_{\text{tip}} \cos \alpha), \\ -\frac{r}{\tan \alpha} + \frac{R_{\text{tip}}}{\sin \alpha} + h_{\text{em}} - R_{\text{tip}}, & (r \geq R_{\text{tip}} \cos \alpha), \end{cases} \quad (18)$$

28 June 2024 00:02:15

where z_{em} represents the axial position of the emitter surface. The needle tip region is described by $0 < r < R_{tip} \cos \alpha$, and the linear surface region is described by $r \geq R_{tip} \cos \alpha$.

The electric field on the porous needle surface E_{surf} was calculated via numerical simulation. The electric field \vec{E} is governed by Gauss's law in integral form,

$$\iint_S -\vec{E} \cdot \vec{n} dS = \iiint_V -\frac{\rho_e}{\epsilon_0} dV, \quad (19)$$

where S represents the surface area of the control volume; \vec{E} represents the electric field; \vec{n} represents the normal vector to the control volume surface; dS represents the area for the area integration; V represents the control volume; ρ_e represents the space charge; and dV represents the volume for the volume integration. The right-hand side of Eq. (19) can be ignored because the space charge is negligible as E_{sc}^* is two orders of magnitude smaller than E^* , where E_{sc}^* represents the electric field induced by the ion cloud surrounding the menisci tips, which is estimated as $E_{sc}^* = \kappa / \epsilon_r \epsilon_0 (mE^* r^* / 2q)^{1/2}$.^{29,30,52} Thus, Eq. (19) is described as Laplace's equation, and the needle surface electric field E_{surf} was calculated numerically via the cut-cell method (Appendix).

Figure 3 shows the typical I - V plots produced by the aforementioned model [Eqs. (16) and (17)] when varying the parameter κ / ϵ_r in Eq. (16). The plots employ an idealized geometric

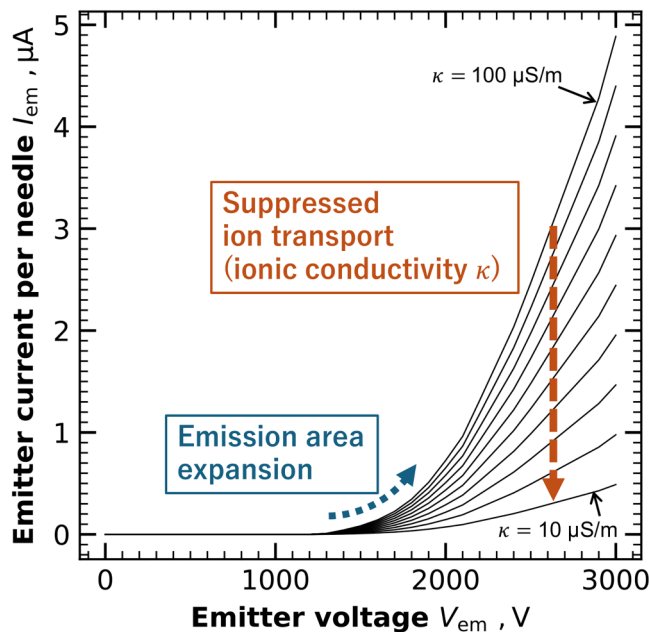


FIG. 3. I - V plots produced by the proposed model using the ideal geometric configuration presented in Table I, with the tip of the emitter needle tip located in the extractor grid plane and $E_{surf,th} = 20 \text{ V}/\mu\text{m}$. The plots are generated by varying the model parameter κ in Eq. (16) from 10–100 $\mu\text{S}/\text{m}$ in increments of 10 $\mu\text{S}/\text{m}$.

TABLE I. Geometry design parameters and the values.

Parameters	Descriptions	Values
h_{em} (mm)	Height of emitter needles	1.0
R_{tip} (μm)	Curvature of emitter needle tips	100
α ($^\circ$)	Half-apex angle of needles	20
r_{ex} (μm)	Radius of extractor holes	400

configuration, listed in Table I, with the tip of the emitter needle located in the extractor grid plane (emitter–extractor gap = 0). Here, ϵ_r is a constant ($\epsilon_r = 8.91$ for EMI-DCA), whereas κ is increased from 10–100 $\mu\text{S}/\text{m}$ in increments of 10 $\mu\text{S}/\text{m}$. Additionally, these plots assume a certain fixed threshold $E_{surf,th} = 20 \text{ V}/\mu\text{m}$ because emission starts when $E_{surf} > E_{surf,th}$. This ion-emission threshold is discussed in Sec. IV. As the surface electric field increases with an increasing voltage, this model indicates that the expansion of the emission area (S_{em}) influences the shape of the I - V curve. Moreover, a decrease in κ , which represents the ion-transport suppression, leads to a reduction in the emitted current, as shown in Fig. 3, where κ was determined using the experimental data presented in Sec. IV.

III. EXPERIMENTAL SETUPS

A. Thruster head configurations

The thruster head consists of a porous emitter and an extractor grid, where porous materials of two different internal scales are used. The first is a 50 nm class porous material manufactured via a standard acid-leaching process,⁵³ and the second is a 7 μm class porous material manufactured via a sintering process (by Nippon Electric Glass Co., Ltd.). Figure 4(a) shows the surface geometry of the emitter array measured with a laser scanning microscope (Keyence, VK-X3000) and design parameters, where h_{em} represents the height of the emitter needles, R_{tip} represents the radius of the needle tips, α represents the half-apex angle of the emitter needle, and r_{ex} represents the radius of the extractor holes. Figure 4(b) shows the photograph taken downstream from one emitter needle and an aligned extractor grid. The alignment error between the needle tip and the center of the extractor grid holes is within 0.03 mm.

The values of these design parameters are presented in Table I. We fabricated multiple needle shapes with a height of 1.0 mm and spacing of 1.0 mm via computer numerical control machining. One emitter array has 76 needles in $1.0 \times 1.0 \text{ cm}^2$ porous media. The grid gap d is adjusted using shim rings between the thruster housing and the extractor grid.

B. Current vs voltage characteristic measurement

The I - V characteristics were measured to determine the total current from the porous emitter. Figure 5 shows the experimental setup used to apply voltages and measure currents. The porous emitter was connected to a source meter (Keithley, 2657A) through a 1 M Ω resistor via the IL, and the extractor grid was connected to another source meter (Keithley, 2612B) through a 100 k Ω resistor.

28 June 2024 00:02:15

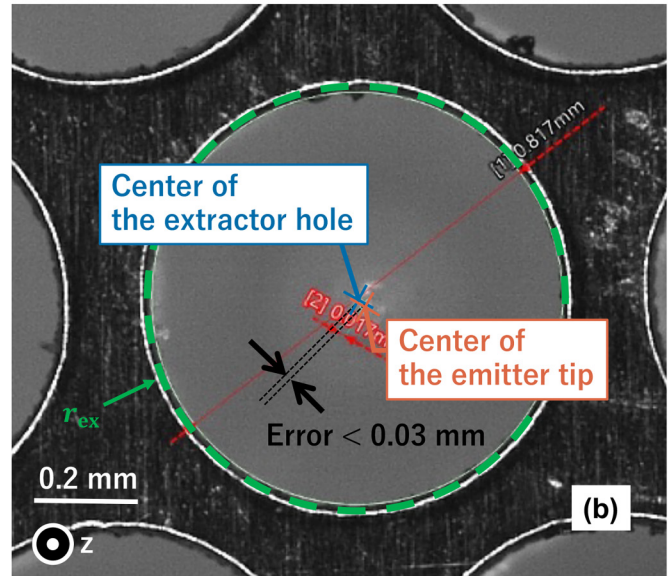
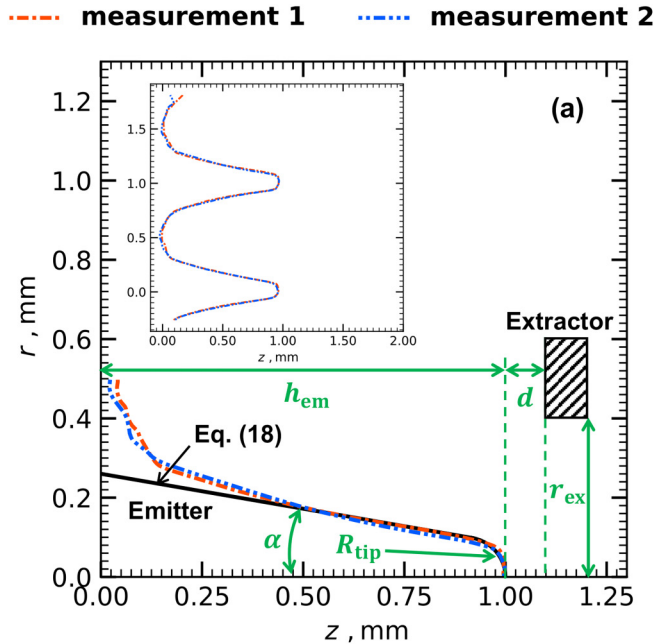


FIG. 4. Thruster head geometry: (a) The surface geometry of the emitter array measured by a laser scanning microscope (Keyence, VK-X3000) and design parameters, where h_{em} represents the height of the emitter needles, R_{tip} represents the radius of the needle tips, α is the half-apex angle of needles, and r_{ex} represents the radius of the extractor holes. (b) A picture taken downstream from one emitter needle and an aligned extractor grid. The alignment error between the needle tip and the center of the extractor hole is within 0.03 mm.

The extractor voltage was fixed at 0 V, and a 1.0 Hz bipolar pulse voltage was applied to the emitter to measure the $I-V$ characteristics. The emitter current was obtained by averaging 60 points with a measurement interval of 10 ms at each applied voltage.

An IL of 1-ethyl-3-methylimidazolium dicyanamide (EMI-DCA) with a molecular weight of 177.23 g/mol was used as the propellant. All measurements were conducted in a vacuum chamber at 5.0×10^{-3} Pa or less. Notably, we only focused on the emitter current to validate the proposed model, but it was also confirmed that the maximum extractor current was less than 10% of the emitter current.

IV. RESULTS AND DISCUSSION

A. Current vs voltage characteristics

Figures 6 and 7 show the $I-V$ characteristics for grid gap d with $7 \mu\text{m}$ class and 50 nm class emitters, respectively. The scattered plots are experimental, and the error bars represent the standard deviation of repeated consecutive data. The emitter current for the 50 nm class and $7 \mu\text{m}$ class emitters has an error of approximately 10%–20% in consecutive operation.

The line plots in Figs. 6 and 7 are calculated using the proposed model [Eqs. (16) and (17)]. The parameter κ/ϵ_r in Eq. (16) was adjusted to fit the calculated $I-V$ characteristics to the experimental data, thereby allowing the determination of κ through the least squares method. Note that $\epsilon_r = 8.91$ (EMI-DCA) is constant, and the parameter estimation is discussed in Sec. IV C. The R^2

value of the least squares method was evaluated, indicating the validity of the fitting. All the R^2 values were larger than 0.95.

In the proposed model, the emitted current density was proportional to $|E_{surf} - E_{surf,th}|$ according to Eq. (16). Thus, if the emission area S_{em} is constant, the emitted current is a linear function of emitter voltage V_{em} , and the $I-V$ characteristics should be linear, where E_{surf} is proportional to V_{em} . However, the emission area expands with an increase in V_{em} , and the emitted current is determined via the area integration of the expanding emission area according to Eq. (17). This emission-area expansion increases the increment rate of the emitted current with an increase in V_{em} . Consequently, the expanding emission area in the increase in the emitter voltage results in the curve shape of the $I-V$ characteristics.

In previous research, two types of $I-V$ characteristics have been reported. In Ref. 18, which considered a geometry similar to that of the emitters examined in this study, the $I-V$ characteristics exhibited a gradual curve shape. The emission area expands with an increase in the emitter voltage. This thruster has a relatively large emitted current owing to multi-site emissions. In Ref. 54, the curve shape of the $I-V$ characteristics changes to a straight line shape in the middle of the range of the increasing emitter voltage. This transition of the $I-V$ characteristics shape indicates that the emission area expands up to the middle of the range of the increasing emitter voltage; however, emission-area expansion is restricted, and the emission area becomes constant as the emitter voltage increases further.

28 June 2024 00:02:15

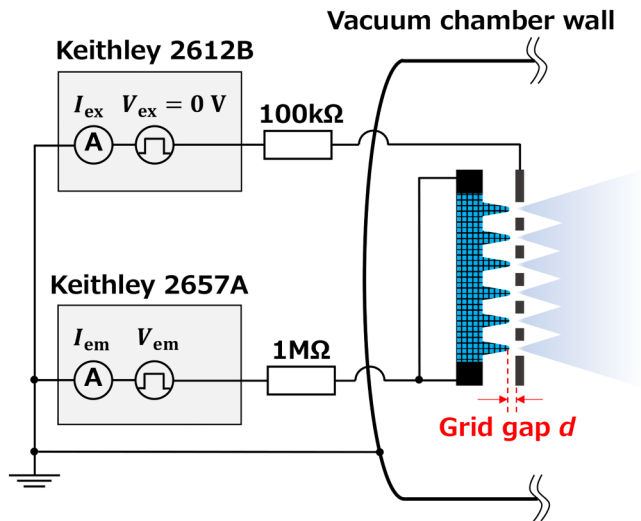


FIG. 5. The experimental setup for applying voltage and measuring current. The porous emitter was connected to a source meter (Keithley, 2657A) through a 1 MΩ resistor via the IL, and the extractor grid was connected to another source meter (Keithley, 2612B) through a 100 kΩ resistor. The extractor voltage was fixed at 0 V, and a 1.0 Hz bipolar pulse voltage was applied to the emitter to measure the I - V characteristics. The emitter current was obtained by averaging 60 points with a measurement interval of 10 ms at each applied voltage.

For the 7 μm class emitter, the shape of the I - V characteristics is successfully reproduced by the proposed model, and the shape is curved with an increase in V_{em} , as shown in Fig. 6. This shape of the I - V characteristics of the 7 μm class emitter corresponds to the case of Ref. 18.

For the 50 nm class emitter, a curve shape is observed up to the middle of the range of the increasing V_{em} and a slightly straighter shape is observed thereafter, as shown in Fig. 7. The shape of the I - V characteristics of the 50 nm class emitter may be restricted in the middle of the range of the increasing V_{em} .

B. Current vs electric field characteristics

Figure 8 shows the experimental results of the current vs electric field (I - E_{tip}) characteristics with 7 μm and 50 nm class emitters for the grid gap. The error magnitude of the repeated experiment is approximately equivalent to the size of the marker [Fig. 8(a) 1 μA and Fig. 8(b) 0.1 μA]. The horizontal axis indicates the maximum value of the surface electric field at the needle tip $E_{surf,r=0}$ in the axial z -direction, and the vertical axis indicates the emitter current per needle I_{em} . The emission starts when a certain electric field $E_{surf,r=0}$ is applied, and the emitted current increases with $E_{surf,r=0}$. The starting point of the curve is evaluated as $E_{surf,th}$. Figure 8 indicates that $E_{surf,th}$ is determined to be 20 V/μm regardless of the

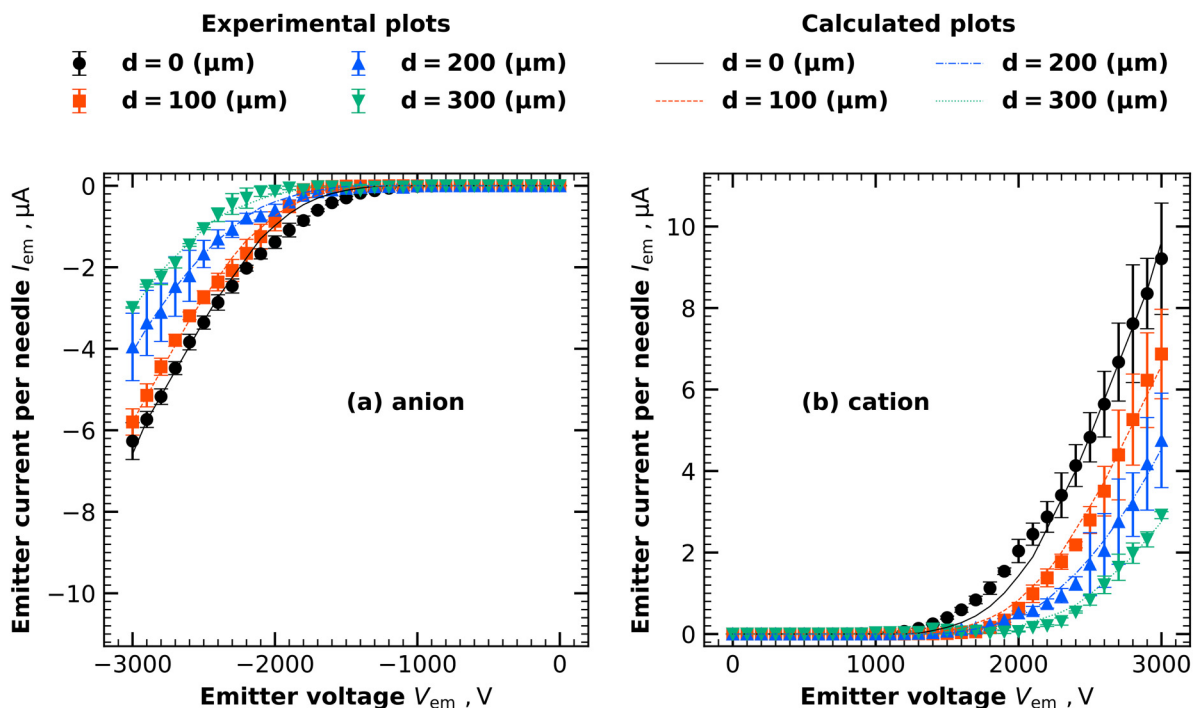


FIG. 6. I - V characteristics in the case of the 7 μm class emitter with grid gap d for (a) anion and (b) cation emission. The scattered plots are experimental, and the error bars represent the standard deviation of repeated consecutive data. The line plots show the results of calculations using the proposed model.

28 June 2024 00:02:15

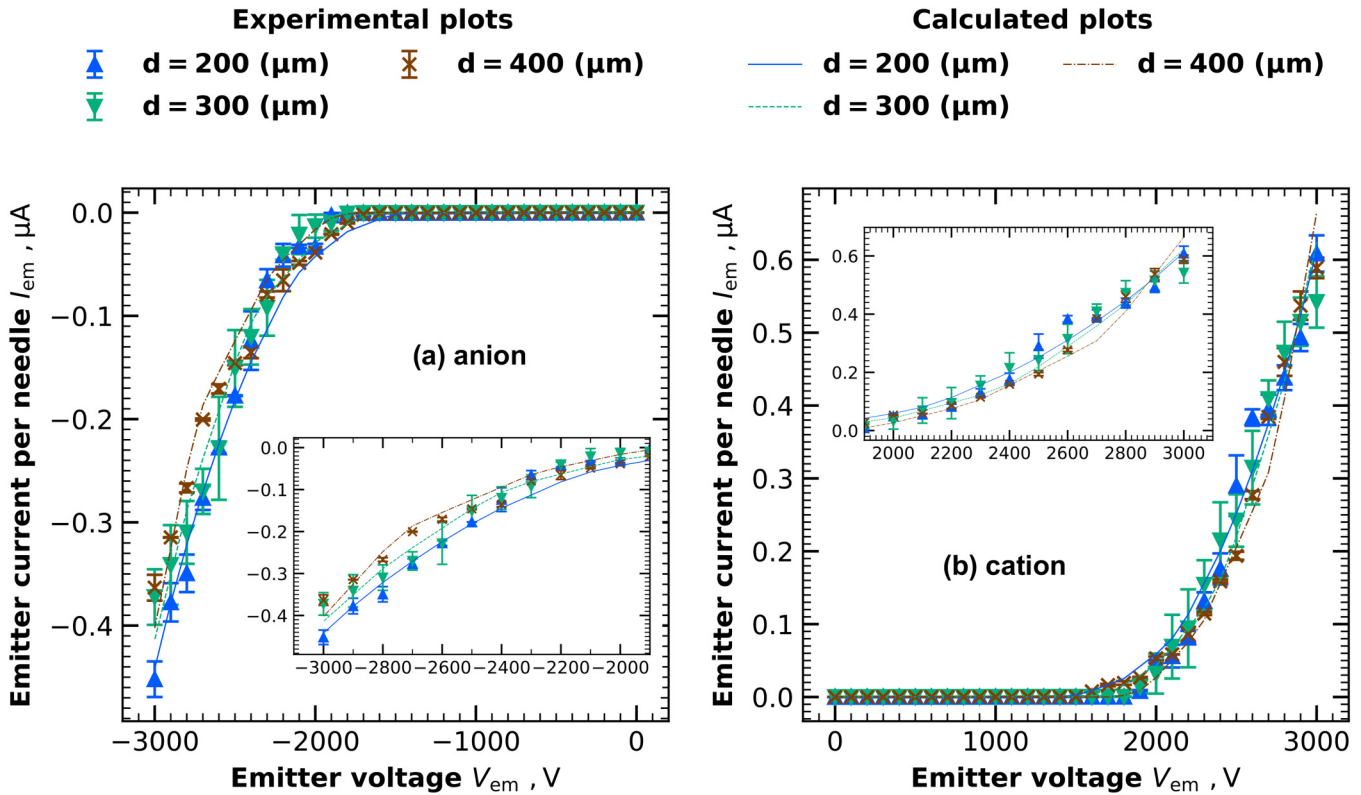


FIG. 7. I - V characteristics in the case of the 50 nm class emitter with grid gap d for (a) anion and (b) cation emission. The scattered plots are experimental, and the error bars represent the standard deviation of repeated consecutive data. The line plots show the results of calculations using the proposed model.

28 June 2024 00:02:15

polarity and porosity. This value was used for the data for the proposed model [Eq. (17)].

Figure 9 shows the two-dimensional distributions of the magnitude of the electric field near the needle tip and the emission area S_{em} for different grid gaps and emitter voltages. The emission area S_{em} is defined as the location where the local E_{surf} exceeds $E_{surf,th} = 20 \text{ V}/\mu\text{m}$ in the proposed model [Eq. (16)], where the direction of E_{surf} is perpendicular to the surface (see Fig. 11 in the Appendix). The emission area increases with an increase in the emitter voltage and a reduction in the grid gap, as shown in Fig. 9. In Fig. 8(a), the emitted current increases with a reduction in the grid gap. Thus, as the gap becomes smaller, the emission area increases, and a large current is emitted from the large emission area (i.e., multi-site emission). If currents are emitted from only one point at the tip (i.e., single-site emission), the I - E_{tip} characteristics should be identical among all the grid gaps.

In Fig. 8(b), the I - E_{tip} characteristics are almost invariable among all the grid gaps. When a 50 nm class emitter is used, the expansion of the emission area may be restricted in the middle of the range of the increasing $E_{tip,r=0}$, as mentioned in Sec. IV A. It is considered that the ion transport is insufficient upstream from the porous needle surface in the case of the 50 nm class emitter.

C. Conductivity

Table II presents the estimated parameter κ . This conductivity was obtained via the fitting process described in Sec. IV A. Thus, the line plots shown in Figs. 6 and 7 represent the values obtained using the numerical model [Eqs. (16) and (17)], employing the parameters listed in Table II.

In addition, the ion-pore wall friction coefficient R_p can be evaluated because R_p and R_l are described with κ as $R_p = (n_i q_i^2)/(m_i \kappa) - R_l \approx (n_0 q_i^2)/(m_{ave} \kappa) - R_l$ using Eqs. (6) and (8). Table II presents the estimated R_p (as R_p/R_l).

For the 7 μm class emitter, the κ of anions and cations can be considered constant within 14% and 6% from their mean values in d . The maximum error of consecutive experiments is approximately 20% of the mean values. Thus, κ is considered constant and independent of the grid gap d . This result of the constant κ implies that there is sufficient ion transport to the porous surface as global flow in the porous emitter and that the emission area expands with an increase in V_{em} , as discussed in Secs. IV A and IV B.

Table II indicates that the ion-pore wall friction R_p is two or three orders of magnitude larger than the ion-ion friction R_l . Thus, the ion-pore wall friction determines the conductivity, and the conductivity determines the emitted current. Here, in particular,

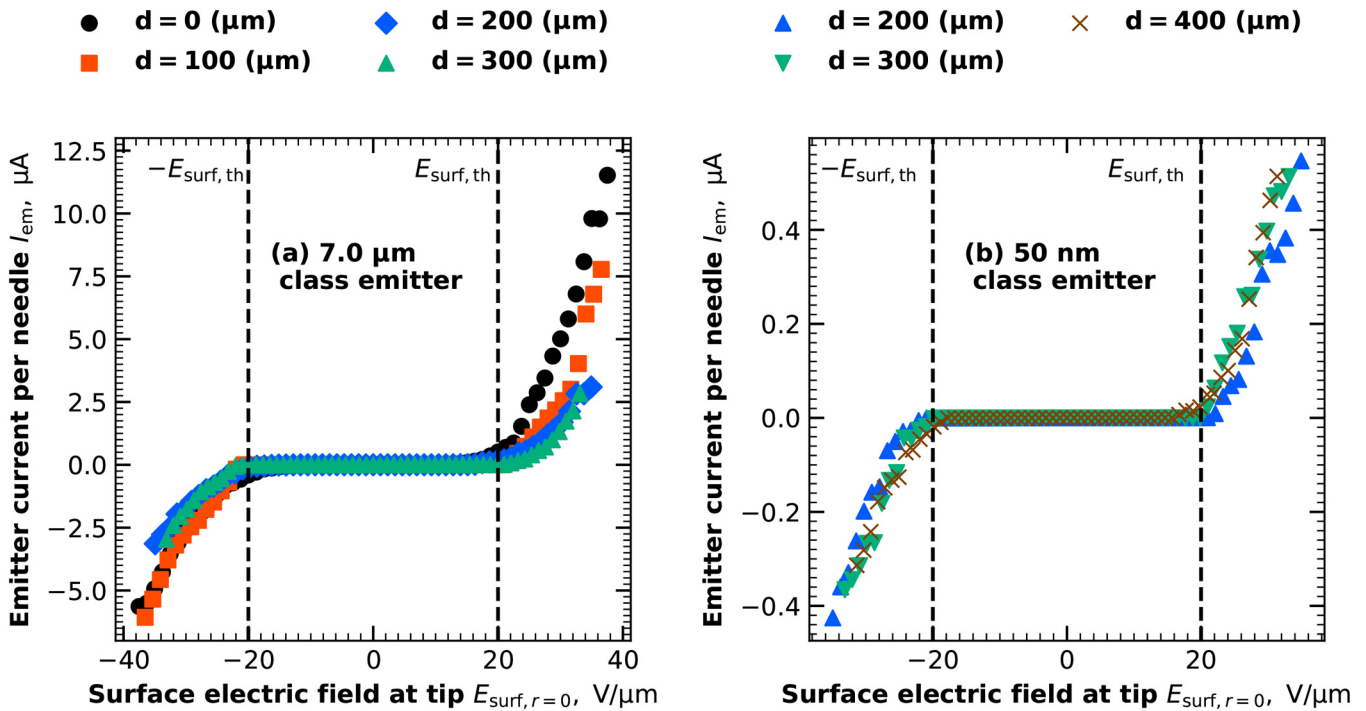


FIG. 8. The experimental results of the current vs needle tip electric field ($I-E_{tip}$) characteristics with (a) 7 μm and (b) 50 nm class emitters for grid gap d . The error magnitude of the repeated experiment is approximately equivalent to the size of the marker [(a) 1 μA and (b) 0.1 μA]. The horizontal axis indicates the surface electric field on the needle tip $E_{surf,r=0}$ in the axial z -direction, and the vertical axis indicates the emitter current per needle I_{em} . The starting point of the curve is evaluated as $E_{surf,th}$.

28 June 2024 00:02:15

ions are current carriers in ILs, and conductivity is based on the mobility of ions as Eq. (8). Moreover, the suppression of conductivity by ion-pore wall friction may play an essential role in ion evaporation (purely ionic regime) because this model indicates that

conductivity κ is related to the flow rate Q as $Q = \kappa E_i S_{cross}/q$, where S_{cross} is a cross section of the flow in a porous emitter, and Q is defined as $I = \rho Q q/m$.^{39,42} The current emitted as the droplet is extinguished and evaporated determines the emitted current when

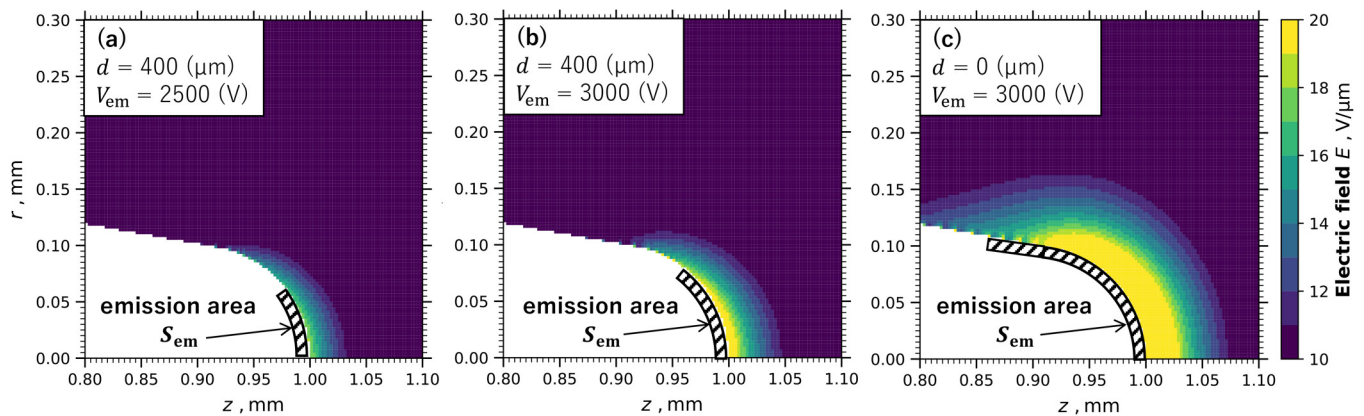


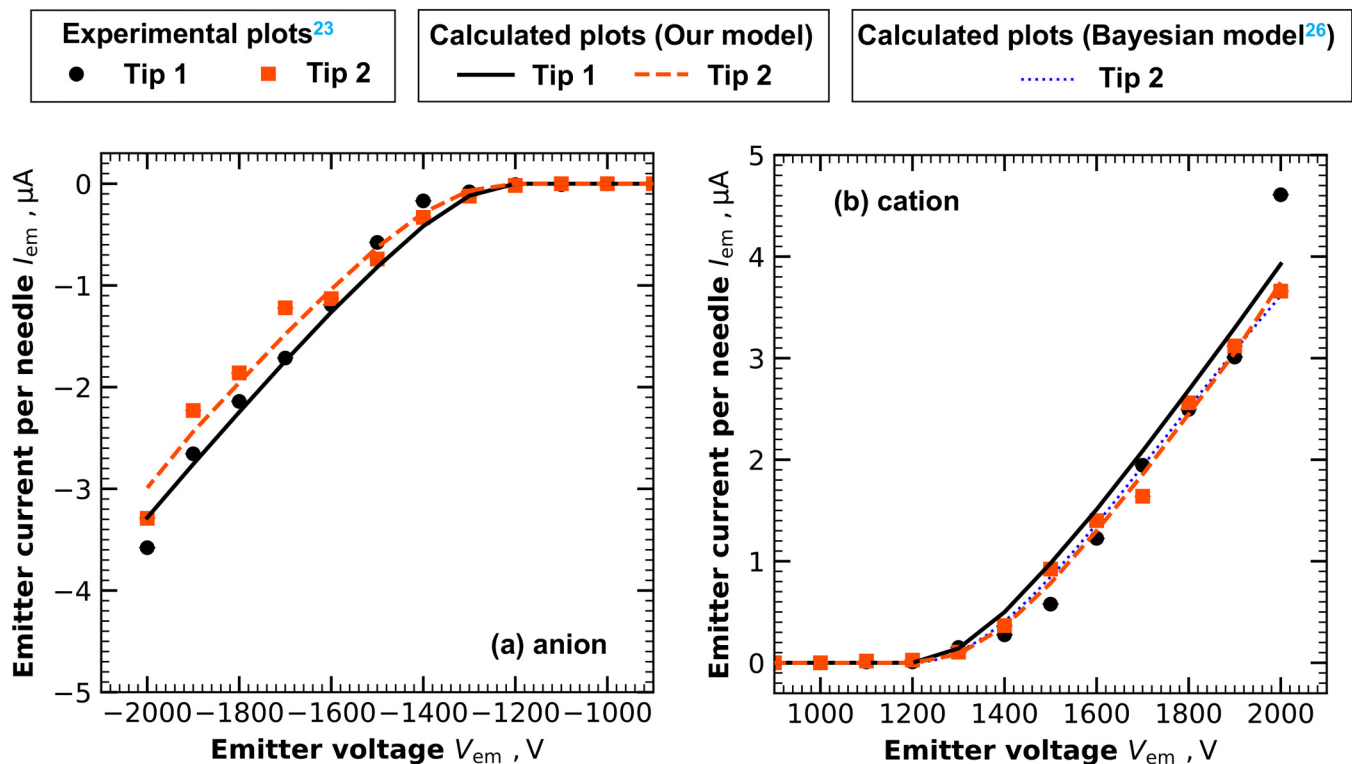
FIG. 9. The two-dimensional distributions of the magnitude of the electric field near the needle tip and the emission area S_{em} for different grid gaps and emitter voltages. The emission area is defined as the location where the local E_{surf} exceeds $E_{surf,th} = 20 V/\mu m$. Three grid gap d and emitter voltage V_{em} conditions are conducted. (a) $d = 400 \mu m$, $V_{em} = 2500 V$, (b) $d = 400 \mu m$, $V_{em} = 3000 V$, and (c) $d = 0 \mu m$, $V_{em} = 3000 V$.

TABLE II. Estimated conductivity κ , the ion-pore wall friction coefficient R_p normalized by the ion-ion friction coefficient R_l using the proposed model for each experimental condition (porosity, polarity, and grid gap).

Porosity	Polarity	d (μm)	κ ($\mu\text{S/m}$)	R_p/R_l
7 μm	Anion (-)	0	140 \pm 7	17 014
		100	151 \pm 9	15 691
		200	159 \pm 35	14 967
		300	209 \pm 3	11 353
7 μm	Cation (+)	0	204 \pm 28	6 912
		100	172 \pm 29	8 200
		200	177 \pm 38	7 972
		300	191 \pm 17	7 379
50 nm	Anion (-)	200	17 \pm 1	138 120
		300	29 \pm 3	82 655
		400	54 \pm 0	43 778
50 nm	Cation (+)	200	24 \pm 1	59 178
		300	43 \pm 4	32 586
		400	90 \pm 2	15 740

the flow rate Q is sufficiently small.^{42,55} Thus, a trade-off may exist: a larger porous scale increases the emitted current owing to the large κ but may induce a droplet regime. This trade-off implies the existence of an optimal porosity for the porous emitter for the large emitted current and the purely ionic regime.

In the case of the 50 nm class emitter, κ depends on experimental conditions. This non-constant κ implies that the emission-area expansion may be restricted in the middle of the range of the increasing V_{em} because of insufficient ion transport to a porous surface, as discussed in Secs. IV A and IV B. The insufficient ion transport as global flow in porous media arises from the porous structure.⁵⁶ The non-constant κ for the various d values is explained as follows. The emitted current I_{em} is calculated via area integration on S_{em} using Eq. (17). However, the actual emission area of the 50 nm class emitter is restricted and smaller than S_{em} from the middle of the range of the increasing V_{em} . Thus, when d is small and S_{em} is calculated to be larger than the actual emission area, the model parameter κ is underestimated as a small value using the measured current I_{em} . In addition, R_p is overestimated for small d values.



28 June 2024 00:02:15

FIG. 10. Application of the proposed model to the experimental data reported in Ref. 22. The result of the Bayesian estimation model (available only for tip 2) from Ref. 25 is also shown for comparison. (a) Anion and (b) cation emissions. The line plots represent the model calculations and the marked plots denote the experimental data.

The emitted current of the $7\ \mu\text{m}$ class emitter exceeds that of the $50\ \text{nm}$ class emitter in Figs. 6 and 7, which is explained by the smaller R_p in the former case. Additionally, the emitted current of the anions is smaller than that of the cations in Figs. 6 and 7. The difficulty in emitting anions has also been reported.¹⁸ This smaller emission current of anions compared with that of cations is also explained by the larger R_p of anions compared with cations. However, the anion emission may be affected by the field emission effect. When a strong negative electric field is applied ($E > 10^9\ \text{V/m}$), the electron cloud is formed around menisci.⁵⁷ The electron cloud shields the electric field and the surface charge and weakens the electric field E_i in the IL, reducing the emitted current density. Thus, κ is evaluated as a smaller value and R_p is evaluated as a larger value in anion emission compared with the cation emission.

D. Model applicability

The proposed model was also applied to experimental data from previous studies. Figure 10 shows its application to the experimental data in Ref. 22, including the plot of a Bayesian estimation model from Ref. 25 for comparison. By analyzing the emitter geometry employed in Ref. 22, we found that the tip curvature R_{tip} is not axially symmetric and varies in the azimuthal directions, that of tip 1 ranging from 17 to $53\ \mu\text{m}$ and tip 2 ranging from 15 to $17\ \mu\text{m}$. However, to calculate the electric fields for the analysis, we assumed the following tip curvatures: $R_{\text{tip}} = 53\ \mu\text{m}$ for tip 1 and $R_{\text{tip}} = 15\ \mu\text{m}$ for tip 2. Moreover, the error bars obtained via repeated experiments and the manufacturing accuracy of the emitter geometry were uncertain in Ref. 22. Thus, the κ evaluation values obtained from Fig. 10 should be considered as approximations (tip 1: $\kappa = 181$ and $216\ \mu\text{S/m}$ for the anion and cation, respectively; tips 2: $\kappa = 951$ and $1192\ \mu\text{S/m}$ for the anion and cation, respectively). Thus, the differences in the tip curvatures of tips 1 and 2 resulted in significant differences in the κ values. As shown in Fig. 10, the proposed model, despite its simplicity, reproduced the I - V shapes as effectively as the Bayesian model.²⁵

V. CONCLUSIONS

A simple model for multi-site emission [Eq. (16)] was proposed based on momentum conservation of transported ions through porous media, with the assumption that conductivity controls ion emission.²⁹ Using the proposed model, the I - V characteristics of experiments were reproduced successfully with a $7\ \mu\text{m}$ class emitter. It is difficult to apply the model to the $50\ \text{nm}$ class emitter because ion transport may be insufficient, and emission-area expansion is restricted with the increasing emitter voltage.

The proposed model indicates that the expansion of the emission area (i.e., multi-site emission) causes the unique curve shape of I - V characteristics.

The ion-ion friction R_l and ion-pore wall friction R_p determine κ . Moreover, the ion-pore friction R_p is the primary factor determining κ because R_p is two orders of magnitude larger than R_l . The larger emitted current for the $7\ \mu\text{m}$ class emitter compared with that for the $50\ \text{nm}$ class emitter is explained by the smaller ion-pore wall friction.

The proposed model assumes that the surface charge converges on the order of magnitude of E_v/ϵ_0 owing to the quasi-neutral region and the non-neutral sheath (double layer) when a strong electric field is applied to the IL ($E_v > E'$). The boundary conditions considering the non-neutral region should be investigated in future research.

ACKNOWLEDGMENTS

This work was partially supported by JSPS KAKENHI under Grant No. JP21H01530, the Canon Foundation, the Advisory Committee for Space Engineering of Japan Aerospace Exploration Agency, Grant-in-Aid for Exploratory Research in the area of human space technology and space exploration, and JST FOREST Program under Grant No. JPMJFR2129. The authors acknowledge Nippon Electric Glass Co., Ltd. for offering porous materials, thank Mr. Takase for fabricating thruster prototypes at the Advanced Machining Technology Group of Japan Aerospace Exploration Agency, and thank Dr. Kazuma Emoto for his insightful reviews and valuable suggestions regarding this paper.

AUTHOR DECLARATIONS

Conflict of Interest

The authors have no conflicts to disclose.

Author Contributions

Koki Takagi: Conceptualization (equal); Data curation (lead); Formal analysis (lead); Investigation (lead); Methodology (lead); Project administration (equal); Software (lead); Validation (lead); Visualization (lead); Writing – original draft (lead); Writing – review & editing (equal). **Yusuke Yamashita:** Conceptualization (equal); Formal analysis (supporting); Methodology (supporting); Software (supporting); Validation (supporting); Writing – review & editing (equal). **Ryudo Tsukizaki:** Funding acquisition (equal); Project administration (equal); Resources (equal); Supervision (equal); Writing – review & editing (equal). **Kazutaka Nishiyama:** Project administration (equal); Resources (equal); Supervision (equal). **Yoshinori Takao:** Funding acquisition (equal); Project administration (equal); Resources (equal); Software (supporting); Supervision (equal); Validation (supporting); Writing – original draft (supporting); Writing – review & editing (equal).

DATA AVAILABILITY

The data that support the findings of this study are available from the corresponding author upon reasonable request.

APPENDIX: DISCRETIZATION

Equation (19) is discretized using second-order central difference methods applicable to the non-surface region, as depicted in Fig. 11(a). A cut-cell method⁵⁸ was applied to calculate the surface electric field E_{surf} on the exact boundary in the surface region depicted in Fig. 11(a). Figure 11(b) shows the control volume for the cut-cell method. E_{surf} , E_T , E_B , and E_R represent the electric fields defined on the left, top, bottom, and right interfaces of the control volume, respectively; Δz represents the distance between

28 June 2024 00:02:15

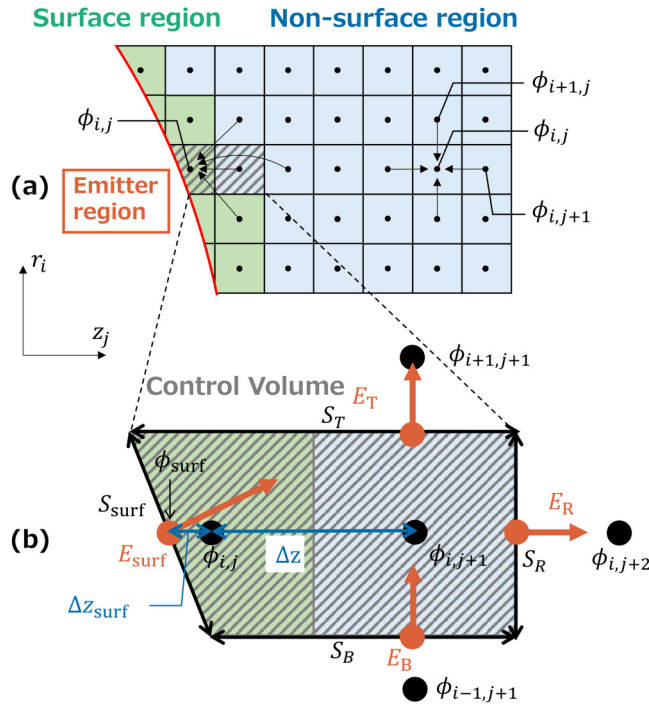


FIG. 11. (a) The cell reference of calculation in the surface and non-surface regions. Electrostatic potential ϕ is defined on the cell center. (b) The control volume for the cut-cell method. E_{surf} , E_T , E_B , and E_R represent the electric fields defined on the left, top, bottom, and right interfaces of the control volume, respectively. Δz represents the distance between cell centers, and Δz_{surf} represents the distance between the exact emitter surface and the cell centers in the surface region.

cell centers; and Δz_{surf} represents the distance between the exact emitter surface and the cell centers in the surface region.

In the surface region, the left-hand side of Eq. (19) is expressed as

$$\iint_S -\vec{E} \cdot \vec{n} dS = -E_{\text{surf}} S_{\text{surf}} + E_R S_R - E_B S_B + E_T S_T, \quad (\text{A1})$$

where S_{surf} , S_T , S_B , and S_R denote the left, top, bottom, and right areas of the control volume, respectively. These electric fields in Eq. (A1) are discretized as

$$\begin{aligned} E_{\text{surf}} &= C_1 \phi_{ij} + C_2 \phi_{i,j+1} + C_3 \phi_{\text{surf}}, \\ E_R &= C_4 \phi_{i,j+2} + C_5 \phi_{i,j+1}, \\ E_B &= C_6 \phi_{i,j+1} + C_7 \phi_{i-1,j+1}, \\ E_T &= C_8 \phi_{i+1,j+1} + C_9 \phi_{i,j+1}, \end{aligned} \quad (\text{A2})$$

where C_1 – C_9 are the coefficients for second-order discretization, which are constructed with Δz , Δz_{surf} , and Δr .

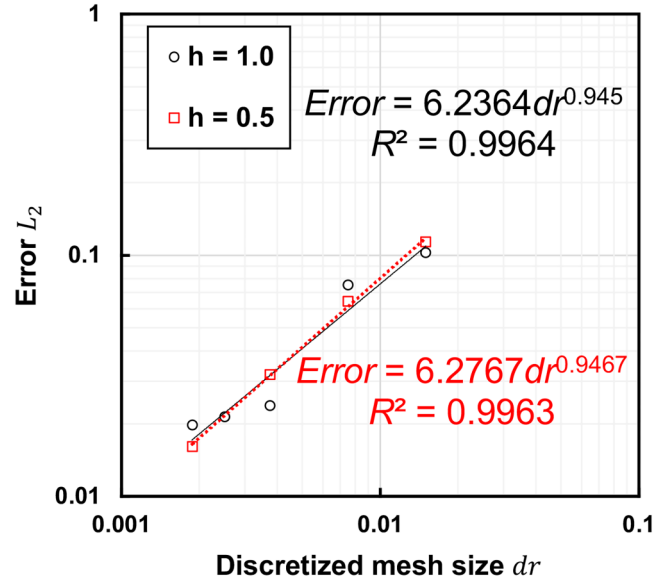


FIG. 12. The result of the L_2 error cell convergence with two emitter height conditions: $h = 0.5$ and 1.0 mm.

The numerical simulation of the surface electric field E_{surf} was verified with the analytical solution. In prolate spheroidal coordinate (η, ξ) , the analytical potential⁵⁹ is expressed as

$$\phi = \phi_0 \frac{\tan^{-1} \eta}{\tan^{-1} \eta_0}, \quad (\text{A3})$$

where

$$\eta = \frac{1}{a} \left[\sqrt{r^2 + \left((z-d) + \frac{a}{2} \right)^2} - \sqrt{r^2 + \left((z-d) - \frac{a}{2} \right)^2} \right], \quad (\text{A4})$$

and $a = 2d(1 + R_{\text{tip}}/d)^{1/2}$. The emitter surface is described as $\eta = \eta_0 = (1 + R_{\text{tip}}/d)^{-1/2}$. The L_2 error⁶⁰ in the needle tip region ($r \leq 0.1$ mm) was evaluated as

$$L_2 = \sqrt{\frac{1}{N_{\text{total}}} \sum_k \frac{(E_{\text{surf},k} - E_{\text{surf,ana},k})^2}{E_{\text{surf,ana},k}^2}}, \quad (\text{A5})$$

where N_{total} represents the total number of cells for the evaluation, $E_{\text{surf},k}$ represents the calculated surface electric field, and $E_{\text{surf,ana},k}$ represents the analytical surface electric field. Figure 12 shows the result of the L_2 error cell convergence with two emitter height conditions: $h = 0.5$ and 1.0 mm. Figure 12 indicates that the numerical calculation of the surface electric field was well-established as approximately first order, i.e., a smaller calculation grid size corresponded to a smaller calculation error. The first-order computational error was observed while Eq. (19) was discretized with the

28 June 2024 00:02:15

second-order accuracy. Non-smoothness of the electric field is observed [e.g., $z < 0.90$ mm in Fig. 9(c)], whereas the electric field is smooth near the tip [e.g., $0.95 < z < 1.00$ mm in Fig. 9(a)]. In this calculation, the control volume is fitted to the emitter surface with a flat shape instead of a curved shape, and E_T and E_B are not defined at the exact center of the control volume surface, which may reduce the calculation order and result in slight non-smoothness.

REFERENCES

- ¹C. D. Hendricks, "Charged droplet experiments," *J. Colloid Sci.* **17**, 249–259 (1962).
- ²J. S. Wilkes, "A short history of ionic liquids—From molten salts to neoteric solvents," *Green Chem.* **4**, 73–80 (2002).
- ³P. Lozano and M. Martínez-Sánchez, "Ionic liquid ion sources: Characterization of externally wetted emitters," *J. Colloid Interface Sci.* **282**, 415–421 (2005).
- ⁴M. Gamero-Castaño and J. Fernández de la Mora, "Direct measurement of ion evaporation kinetics from electrified liquid surfaces," *J. Chem. Phys.* **113**, 815–832 (2000).
- ⁵D. G. Courtney, H. Q. Li, and P. Lozano, "Emission measurements from planar arrays of porous ionic liquid ion sources," *J. Phys. D: Appl. Phys.* **45**, 485203 (2012).
- ⁶R.-H. Jimmy, J. Iulia, F. Dakota, K. David, F. Corey, and L. Paulo, "Porous materials for ion-electrospray spacecraft microengines," *J. Nanomech. Microtech.* **7**, 04017006 (2017).
- ⁷M. Gomez Jenkins, D. Krejci, and P. Lozano, "CubeSat constellation management using ionic liquid electrospray propulsion," *Acta Astronaut.* **151**, 243–252 (2018).
- ⁸M. Gamero-Castano and V. Hruby, "Electrospray as a source of nanoparticles for efficient colloid thrusters," *J. Propul. Power* **17**, 977–987 (2001).
- ⁹S. Dandavino, C. Ataman, C. N. Ryan, S. Chakraborty, D. Courtney, J. P. W. Stark, and H. Shea, "Microfabricated electrospray emitter arrays with integrated extractor and accelerator electrodes for the propulsion of small spacecraft," *J. Micromech. Microeng.* **24**, 075011 (2014).
- ¹⁰K. Suzuki, M. Nagao, Y. Liu, K. Murakami, S. Khumpuang, S. Hara, and Y. Takao, "Fabrication of nano-capillary emitter arrays for ionic liquid electrospray thrusters," *Jpn. J. Appl. Phys.* **60**, SCCF07 (2021).
- ¹¹B. Gassend, L. F. Velasquez-Garcia, A. I. Akinwande, and M. Martinez-Sanchez, "A microfabricated planar electrospray array ionic liquid ion source with integrated extractor," *J. Microelectromech. Syst.* **18**, 679–694 (2009).
- ¹²F. Tachibana, T. Tsuchiya, and Y. Takao, "Uniform needle-emitter arrays for ionic liquid electrospray thrusters with precise thrust control," *Jpn. J. Appl. Phys.* **60**, SCCL06 (2021).
- ¹³D. Courtney, H. Li, P. Lozano, P. GomezMaqueo, and T. Fedkiw, "On the validation of porous nickel as substrate material for electrospray ion propulsion," in *46th AIAA/ASME/SAE/ASEE Joint Propulsion Conference & Exhibit*, Joint Propulsion Conferences (American Institute of Aeronautics and Astronautics, Reston, VA, 2010).
- ¹⁴C. S. Coffman and P. C. Lozano, "On the manufacturing and emission characteristics of dielectric electrospray sources," in *49th AIAA/ASME/SAE/ASEE Joint Propulsion Conference* (American Institute of Aeronautics and Astronautics, Reston, VA, 2013), Vol. 1 Part F.
- ¹⁵D. G. Courtney, S. Dandavino, and H. Shea, "Comparing direct and indirect thrust measurements from passively fed ionic electrospray thrusters," *J. Propul. Power* **32**, 392–407 (2016).
- ¹⁶M. R. Natisin, H. L. Zamora, W. A. McGehee, N. I. Arnold, Z. A. Holley, M. R. Holmes, and D. Eckhardt, "Fabrication and characterization of a fully conventionally machined, high-performance porous-media electrospray thruster," *J. Micromech. Microeng.* **30**, 115021 (2020).
- ¹⁷C. Ma, "Design and characterisation of electrospray thrusters with high emission density," Ph.D. thesis (University of Southampton, 2020).
- ¹⁸C. Ma, T. Bull, and C. N. Ryan, "Plume composition measurements of a high-emission-density electrospray thruster," *J. Propul. Power* **37**, 816–831 (2021).
- ¹⁹C. S. Perez-Martinez and P. C. Lozano, "Ion field-evaporation from ionic liquids infusing carbon xerogel microtips," *Appl. Phys. Lett.* **107**, 043501 (2015).
- ²⁰O. Jia-Richards, "Quantification of ionic-liquid ion source beam composition from time-of-flight data," *J. Appl. Phys.* **132**, 074501 (2022).
- ²¹P. L. Wright and R. E. Wirz, "Multiplexed electrospray emission on a porous wedge," *Phys. Fluids* **33**, 012003 (2021).
- ²²R. A. Dressler, B. St. Peter, Y.-H. Chiu, and T. Fedkiw, "Multiple emission sites on porous glass electrospray propulsion emitters using dielectric propellants," *J. Propul. Power* **38**, 809–821 (2022).
- ²³Z. Liu, K. Hara, and M. N. Shneider, "Dynamics of electrified liquid metal surface using shallow water model," *Phys. Fluids* **35**, 042101 (2023).
- ²⁴B. S. Peter, R. A. Dressler, Y.-H. Chiu, and T. Fedkiw, "Electrospray propulsion engineering toolkit (ESPET)," *Aerospace* **7**, 91 (2020).
- ²⁵C. B. Whittaker and B. A. Jorns, "Modeling multi-site emission in porous electrosprays resulting from variable electric field and meniscus size," *J. Appl. Phys.* **134**, 083301 (2023).
- ²⁶E. M. Petro, X. Gallud, S. K. Hampl, M. Schroeder, C. Geiger, and P. C. Lozano, "Multiscale modeling of electrospray ion emission," *J. Appl. Phys.* **131**, 193301 (2022).
- ²⁷J. Asher, Z. Huang, C. Cui, and J. Wang, "Multi-scale modeling of ionic electrospray emission," *J. Appl. Phys.* **131**, 014902 (2022).
- ²⁸K. J. Terhune, L. B. King, K. He, and J. Cumings, "Radiation-induced solidification of ionic liquid under extreme electric field," *Nanotechnology* **27**, 375701 (2016).
- ²⁹F. J. Higuera, "Model of the meniscus of an ionic-liquid ion source," *Phys. Rev. E* **77**, 026308 (2008).
- ³⁰C. S. Coffman, M. Martínez-Sánchez, and P. C. Lozano, "Electrohydrodynamics of an ionic liquid meniscus during evaporation of ions in a regime of high electric field," *Phys. Rev. E* **99**, 063108 (2019).
- ³¹J. V. Iribarne and B. A. Thomson, "On the evaporation of small ions from charged droplets," *J. Chem. Phys.* **64**, 2287–2294 (1976).
- ³²I. G. Loscertales and J. Fernández de la Mora, "Experiments on the kinetics of field evaporation of small ions from droplets," *J. Chem. Phys.* **103**, 5041–5060 (1995).
- ³³A. Castellanos, *Electrohydrodynamics* (Springer Science & Business Media, 1998).
- ³⁴J. H. van Lopik, R. Snoeijers, T. C. G. W. van Dooren, A. Raouf, and R. J. Schotting, "The effect of grain size distribution on nonlinear flow behavior in sandy porous media," *Transp. Porous Media* **120**, 37–66 (2017).
- ³⁵H. F. George and F. Qureshi, "Newton's law of viscosity, Newtonian and non-Newtonian fluids," in *Encyclopedia of Tribology*, edited by Q. J. Wang and Y.-W. Chung (Springer US, Boston, MA, 2013), pp. 2416–2420.
- ³⁶R. Zhou, C. Sun, and B. Bai, "Wall friction should be decoupled from fluid viscosity for the prediction of nanoscale flow," *J. Chem. Phys.* **154**, 074709 (2021).
- ³⁷D. R. MacFarlane, M. Forsyth, E. I. Izgorodina, A. P. Abbott, G. Annat, and K. Fraser, "On the concept of ionicity in ionic liquids," *Phys. Chem. Chem. Phys.* **11**, 4962–4967 (2009).
- ³⁸K. Ueno, H. Tokuda, and M. Watanabe, "Ionicity in ionic liquids: Correlation with ionic structure and physicochemical properties," *Phys. Chem. Chem. Phys.* **12**, 1649–1658 (2010).
- ³⁹X. Gallud and P. C. Lozano, "The emission properties, structure and stability of ionic liquid menisci undergoing electrically assisted ion evaporation," *J. Fluid Mech.* **933**, A43 (2022).
- ⁴⁰C. Coffman, "Electrically-assisted evaporation of charged fluids: Fundamental modeling and studies on ionic liquids," Ph.D. thesis (Massachusetts Institute of Technology, 2016).
- ⁴¹L. D. Landau, E. M. Lifshitz, and L. P. Pitaevskii, in *Electrodynamics of Continuous Media*, Course of Theoretical Physics, 2nd ed. (Butterworth-Heinemann, Oxford, 1984).

- ⁴²X. Gallud and P. C. Lozano, “The limited effect of electric conductivity on the ion current evaporated from electrospray sources,” [arXiv:2305.14714](https://arxiv.org/abs/2305.14714) (2012).
- ⁴³C. Chen, Y. Fan, G. Xia, C. Lu, B. Sun, and Y. Han, “Ion evaporation-induced tip streaming from liquid drops of ionic liquids,” *Phys. Fluids* **36**, 032013 (2024).
- ⁴⁴M. Z. Bazant, B. D. Storey, and A. A. Kornyshev, “Double layer in ionic liquids: Overscreening versus crowding,” *Phys. Rev. Lett.* **106**, 046102 (2011).
- ⁴⁵M. S. Kilic, M. Z. Bazant, and A. Ajdari, “Steric effects in the dynamics of electrolytes at large applied voltages. I. Double-layer charging,” *Phys. Rev. E* **75**, 021502 (2007).
- ⁴⁶M. S. Kilic, M. Z. Bazant, and A. Ajdari, “Steric effects in the dynamics of electrolytes at large applied voltages. II. Modified Poisson-Nernst-Planck equations,” *Phys. Rev. E* **75**, 021503 (2007).
- ⁴⁷M. A. Gebbie, H. A. Dobbs, M. Valtiner, and J. N. Israelachvili, “Long-range electrostatic screening in ionic liquids,” *Proc. Natl. Acad. Sci. U.S.A.* **112**, 7432–7437 (2015).
- ⁴⁸M. A. Gebbie, M. Valtiner, X. Banquy, E. T. Fox, W. A. Henderson, and J. N. Israelachvili, “Ionic liquids behave as dilute electrolyte solutions,” *Proc. Natl. Acad. Sci. U.S.A.* **110**, 9674–9679 (2013).
- ⁴⁹S. Tsuzuki, H. Tokuda, K. Hayamizu, and M. Watanabe, “Magnitude and directionality of interaction in ion pairs of ionic liquids: Relationship with ionic conductivity,” *J. Phys. Chem. B* **109**, 16474–16481 (2005).
- ⁵⁰J. Vila, P. Ginés, J. M. Pico, C. Franjo, E. Jiménez, L. M. Varela, and O. Cabeza, “Temperature dependence of the electrical conductivity in EMIM-based ionic liquids: Evidence of Vogel–Tamman–Fulcher behavior,” *Fluid Phase Equilib.* **242**, 141–146 (2006).
- ⁵¹C. Schreiner, S. Zugmann, R. Hartl, and H. J. Gores, “Fractional Walden rule for ionic liquids: Examples from recent measurements and a critique of the so-called ideal KCl line for the Walden plot,” *J. Chem. Eng. Data* **55**, 1784–1788 (2010).
- ⁵²K. Emoto, T. Tsuchiya, and Y. Takao, “Numerical investigation of steady and transient ion beam extraction mechanisms for electrospray thrusters,” *Trans. Jpn. Soc. Aeronaut. Space Sci. Aerosp. Technol. Jpn.* **16**, 110–115 (2018).
- ⁵³M. Kukizaki and T. Nakashima, “Acid leaching process in the preparation of porous glass membranes from phase-separated glass in the Na₂O–CaO–MgO–Al₂O₃–B₂O₃–SiO₂ system,” *Membranes* **29**, 301–308 (2004).
- ⁵⁴D. Krejci, F. Mier-Hicks, R. Thomas, T. Haag, and P. Lozano, “Emission characteristics of passively fed electrospray microthrusters with propellant reservoirs,” *J. Spacecr. Rockets* **54**, 447–458 (2017).
- ⁵⁵I. Romero-Sanz, R. Bocanegra, J. Fernandez de la Mora, and M. Gamero-Castaño, “Source of heavy molecular ions based on Taylor cones of ionic liquids operating in the pure ion evaporation regime,” *J. Appl. Phys.* **94**, 3599–3605 (2003).
- ⁵⁶U. Eberhard, H. J. Seybold, E. Secchi, J. Jiménez-Martínez, P. A. Rühls, A. Ofner, J. S. Andrade, Jr., and M. Holzner, “Mapping the local viscosity of non-Newtonian fluids flowing through disordered porous structures,” *Sci. Rep.* **10**, 11733 (2020).
- ⁵⁷R. H. Fowler and L. Nordheim, “Electron emission in intense electric fields,” *Proc. R. Soc. London A* **119**, 173–181 (1928).
- ⁵⁸D. M. Ingram, D. M. Causon, and C. G. Mingham, “Developments in cartesian cut cell methods,” *Math. Comput. Simul.* **61**, 561–572 (2003).
- ⁵⁹P. D. Prewett and G. L. R. Mair, *Focused Ion Beams from Liquid Metal Ion Sources* (Wiley, 1991).
- ⁶⁰A. S. Chamarthi, K. Komurasaki, and R. Kawashima, “High-order upwind and non-oscillatory approach for steady state diffusion, advection–diffusion and application to magnetized electrons,” *J. Comput. Phys.* **374**, 1120–1151 (2018).